Applied Catalysis B: Environmental 324 (2023) 122239

Contents lists available at ScienceDirect

Applied Catalysis B: Environmental

journal homepage: www.elsevier.com/locate/apcatb

Mapping a thermodynamic stability window to prevent detrimental reactions during CO_2 electrolysis in solid oxide electrolysis cells

Shiqing Hu [a,c], Bingjie Pang [a], Liming Zhang [a,b], Zhongwei Cao [a], Peng Zhang [a], Yunjie Ding [c], Ryan O'Hayre [d,*], Xuefeng Zhu [a,b,**], Weishen Yang [a,b]

[a] State Key Laboratory of Catalysis, Dalian Institute of Chemical Physics, Chinese Academy of Sciences, Dalian 116023, Liaoning, China
[b] University of Chinese Academy of Sciences, Beijing 100049, China
[c] Dalian National Laboratory for Clean Energy, Dalian Institute of Chemical Physics, Chinese Academy of Sciences, Dalian 116023, Liaoning, China
[d] Department of Metallurgical and Materials Engineering, Colorado School of Mines, 1500 Illinois Street, Golden 80401, USA

ARTICLE INFO

Keywords:
Carbon deposition
Carbon dioxide fixation
Thermodynamic analysis
Nickel oxidation
Solid oxide electrolysis cell

ABSTRACT

Preventing Ni oxidation and carbon deposition, regarded as two major issues for CO_2 electrolysis with conventional Ni-based cathodes, is a critical challenge for the development of solid oxide electrolysis cells (SOECs). However, the origin of these two detrimental reactions remains unclear. Here, we unveil that the Nernst voltage, in relation to the operating voltage applied to the SOEC, is the determining factor in controlling these electrochemical reactions. This insight enables the establishment of a reaction phase diagram that identifies the temperature-dependent operating voltage window where both Ni oxidation and carbon deposition can be avoided. We construct this reaction phase diagram based on the results of experiments and a thermodynamic model, and we validate it at a typical reaction condition (cathode: CO_2, 1 atm; anode: air, 1 atm; temperature: 800 °C). As a result, pure CO_2 electrolysis in Ni-based cathode supported SOECs is successfully demonstrated without Ni oxidation and carbon deposition.

1. Introduction

In the context of the ongoing global energy transformation to reduce CO_2 emissions, renewable electricity is increasingly thriving.[1-3] While certain sectors of the energy economy can be directly supported by renewables, displacing hard-to-decarbonize sectors such as aviation fuels or plastics requires carbon-neutral hydrocarbon feedstock inputs.[4-6] Here, CO_2 electrolysis via solid oxide electrolysis cells (SOECs) to produce carbon-neutral syngas (a feedstock for chemicals or fuels production) is considered particularly attractive as it offers high efficiency and conversion.[7] In SOEC-based CO_2 electrolysis, CO_2 is electrolyzed into CO and O^{2-} on cathode, then O^{2-} migrates through the electrolyte and forms O_2 on anode. As they offer good activity, low cost and scalability, Ni-YSZ (Y_2O_3 stabilized ZrO_2) cathode supported SOECs (Ni-SOECs) have been widely studied from the button cell to the stack scale for CO_2 electrolysis [8-10].

Generally, the NiO-YSZ cathode is first reduced to Ni-YSZ under flowing H_2 before electrolysis operation, as direct reduction under CO_2 is infeasible. The reduction process ensures percolating electronic conductivity through the cathode and creates triple phase boundaries (TPBs, Ni/YSZ/gas) as active sites for electrochemical reaction. After reduction, reductively protective "safe" gases, such as H_2 or CO, are continuously added into the CO_2 stream to prevent re-oxidation of Ni during electrolysis operation. Ni oxidation disrupts the electronic conductivity and creates mechanical stress, thus decreasing cathode activity and leading, in some cases, to catastrophic mechanical failure of the SOEC.[11-13] The use of safe gas protection is effective, but it increases the complexity of the SOEC system and decreases efficiency. In addition to safe-gas protection, Ni alloying is also sometimes implemented to reduce surface oxygen affinity and enhance the redox durability of the Ni-based cathode since high oxygen affinity is commonly considered the driver of metal oxidation.[11,14] However, the reduction of oxygen affinity imparted by alloying elements can simultaneously weaken the catalytic activity of Ni towards CO_2. Recently, stable pure CO_2 electrolysis at − 1.5 V and 700 °C in a pure Ni-SOEC for 60 h has been reported, implying that the Ni metal state can be maintained during CO_2

* Corresponding author.
** Corresponding author at: State Key Laboratory of Catalysis, Dalian Institute of Chemical Physics, Chinese Academy of Sciences, Dalian 116023, Liaoning, China.
E-mail addresses: rohayre@mines.edu (R. O'Hayre), zhuxf@dicp.ac.cn (X. Zhu).

https://doi.org/10.1016/j.apcatb.2022.122239
Received 26 October 2022; Received in revised form 13 November 2022; Accepted 28 November 2022
Available online 29 November 2022

electrolysis.[15] Therefore, identifying the correlation between Ni oxidation behavior and electrolysis conditions is urgently needed so that operating strategies for stable CO_2 electrolysis can be designed.

Carbon deposition, which causes catalyst deactivation and interface delamination, is recognized as another crucial challenge for long-term stable CO_2 electrolysis in Ni-SOECs. Carbon deposition on Ni-based cathodes has been widely investigated with a variety of characterization methods.[16-18] Carbon species commonly accumulate at TPBs near the cathode/electrolyte interface.[19] Although many efforts have been made to enhance the coking resistance of Ni catalysts, such as support alteration and surface engineering by infiltration or exsolution, [20-22] carbon deposition is still observed under harsh electrolysis conditions.[17,23] Mogensen et al. attributed carbon deposition to gas diffusion limitations leading to severe local gas composition inhomogeneities in the electrode structure.[24] In comparing Ni-YSZ with a Ni-Sm-doped CeO_2 (SDC) cathode, Skafte et al. proposed that the lack of oxidized carbon intermediates plays a crucial role in carbon build-up on Ni-YSZ during CO_2 electrolysis.[17] Finally, the Yildiz group has identified metal atomic valence as a crucial factor in determining the presence or absence of carbon deposition during CO_2 electrolysis.[25] As illustrated by the diversity of these various hypotheses, it is clear that the origin(s) and mechanism(s) of carbon deposition are still under investigation and more work is needed to understand them.

At present, several mathematical models have been built to interpret the relationship between cathode microstructure, mass transport, and electrochemical performance.[26-28] Most of them are complex and based on detailed fluid dynamics modeling, yet they cannot disclose the origins of Ni oxidation and carbon deposition. Both Ni oxidation and carbon deposition are chemical reactions. The relative favorability of these reactions is therefore determined by the direction and magnitude of their deviation from thermodynamic equilibrium. Thus, the origin of Ni oxidation and carbon deposition on Ni-YSZ cathode can, in principle, be intrinsically understood via thermodynamic considerations using the difference between the chemical potential of reacting species (as captured by the Nernst voltage) versus the applied operating voltage of the electrolysis cell to determine the thermodynamic favorability of these processes.

Herein, we analyze the voltage distribution and establish a thermodynamic model to better understand the electrochemical stability boundaries of the CO_2 electrolysis process in Ni-SOECs. Thermodynamic analysis reveals that the Nernst voltage, in relation to the applied electrolysis voltage, is the determining factor in controlling Ni oxidation and carbon deposition. As a result, it is possible to construct a "reaction phase diagram" that reveals an operational electrolysis voltage window (under certain input gas conditions), where both Ni oxidation and carbon deposition can be simultaneously inhibited during pure CO_2 electrolysis.

2. Experimental

2.1. Cells fabrication and electrochemical tests

NiO-YSZ cathode supported SOECs without anode (NiO-YSZ (~400 μm)|YSZ (~10 μm), Φ = 18 mm) were purchased from Ningbo SOFCMAN Energy Co. Ltd. Cross-section scanning electron microscope (SEM) images of a representative SOEC is provided in Fig. S1. A circular Pt anode, 8 mm in diameter, was brushed on the YSZ electrolyte surface, yielding an effective electrode area of 0.5 cm^2. After drying the Pt anode under infrared light, the SOECs were sealed on a home-made testing device (Fig. S2) and heated up to 800 °C.

SOECs fabricated in this fashion were evaluated via two-electrode electrochemical measurement method at 800 °C—in some cases the cells were first reduced in flowing H_2 at temperature to convert the NiO to Ni metal prior to testing. In other cases, pre-reduction was not conducted. A baseline reaction condition typical for CO_2 electrolysis was selected (cathode: CO_2, 1 atm; anode: air, 1 atm). A high air flow rate (100 mL min^{-1}, the upper limit of the mass flowmeter) was supplied to the anode side in order to mitigate as much as possible any concentration polarization effects, while a CO_2 flow rate of 50 mL min^{-1} was fed to the cathode side. The polarization curves (*I-V*) were collected at a scan rate of 5 mV min^{-1}. Electrochemical impedance spectra (EIS) were measured at different DC bias voltages with a sinusoidal AC perturbation amplitude of 10 mV in the frequency range from 10^5 to 0.1 Hz. The outlet gas composition was analyzed by gas chromatography (Agilent 7890) for the calculation of Faradaic efficiency. The detailed calculation procedures and the related experimental data are provided in Section 1 of the supplementary information (SI).

2.2. Characterizations

X-ray diffraction (XRD): The cathode phase structure was characterized by XRD (PANalytical Empyrean-100 diffractometer equipped with Cu Kα (λ = 1.54 Å) at 40 kV and 40 mA. The diffraction patterns were collected in the range of 2θ = 10–80° at a scanning rate of 10° min^{-1}.

Scanning electron microscopy (SEM): The cathode microstructure and elemental mapping images were acquired using a scanning electron microscope (JSM-7900 F) equipped with an energy dispersive X-ray spectroscopy detector. SEM images obtained on a FEI Quata 200 F were also used in this work.

Raman spectroscopy: The possible carbon deposition after electrochemical test was evaluated by Raman spectroscopy (LabRAM HR 800 Raman spectrometer) equipped with a green laser (532 nm wavelength).

3. Results and discussion

3.1. Possible reactions during CO_2 electrolysis in SOECs

To calculate whether there is a rational voltage window where Ni oxidation and carbon deposition can be avoided, the possible (electro) chemical reactions that may occur during CO_2 electrolysis in a SOEC should be elucidated.

3.1.1. CO_2 electrolysis

The target reaction for CO_2 electrolysis is shown in reaction (1):

$$2\,CO_2 = 2CO + O_2 \quad (1)$$

3.1.2. NiO reduction

The possible pathways for NiO reduction to Ni are shown in reactions (2) and (3). Reaction (2) represents the direct electro-reduction of NiO (oxygen is evolved on the anode side of the cell), while reaction (3) is the thermochemical reduction of NiO due to the existence of CO produced during CO_2 electrolysis.

$$2NiO = 2Ni + O_2 \quad (2)$$

$$NiO + CO = Ni + CO_2 \quad (3)$$

3.1.3. Carbon deposition

There are three possible reactions for carbon deposition, namely deep electro-reduction of CO_2 (reaction 4), CO electro-reduction (reaction 5) and CO disproportionation reaction (reaction 6).

$$CO_2 = C + 2\,O_2 \quad (4)$$

$$2CO = 2\,C + O_2 \quad (5)$$

$$2CO = CO_2 + C \quad (6)$$

It is well-known that reaction spontaneity is decided by thermody-

namic considerations, i.e. specifically, the Gibbs free energy for the reaction process, $\Delta G < 0$. For a generic reaction (e.g., reaction (7), below), ΔG can be obtained by Eq. (8) as:

$$aA(g) + bB(g) = cC(g) + dD(g) \quad (7)$$

$$\Delta G(T) = \Delta G^{\theta}(T) + RT\ln\left[\frac{\left(\frac{P_C}{P_0}\right)^c \bullet \left(\frac{P_D}{P_0}\right)^d}{\left(\frac{P_A}{P_0}\right)^a \bullet \left(\frac{P_B}{P_0}\right)^b}\right] \quad (8)$$

Where, T is the thermodynamic temperature; R is the ideal gas constant; $\Delta G^{\theta}(T)$ is the standard Gibbs free energy; P_x (x = A, B, C and D) is partial pressure of gas x and P_0 is the standard atmospheric pressure.

3.2. Thermodynamic model for CO_2 electrolysis in SOECs

Firstly, it is supposed that a reaction steady-state is established when a given electrolysis voltage (E_{appl}) is applied. This means CO and O_2 are produced at a constant rate, resulting in a specific CO/CO_2 composition at the cathode and a specific oxygen partial pressure at the anode. The resulting steady-state gas compositions under E_{appl} sets the Nernst voltage (E_N) for the cell, due to the difference of oxygen chemical potential between anode and cathode, which, crucially, is different (higher, under electrolysis operation) from the Nernst voltage of the cell at OCV. Fig. 1 schematically illustrates the voltage distribution and sources of voltage loss across a SOEC. During electrolysis, the E_{appl} counteracts the E_N as well as the various voltage losses occurring at the anode (η_a), electrolyte (η_Ω) and cathode (η_c). The E_N is determined by the temperature of the cell and the gas compositions at the cathode and the anode. The relationship between E_{appl} and these various voltage losses can be described via Eq. (9):

$$E_{appl} = E_N + \eta_a + \eta_\Omega + \eta_c = E_N + E_{loss} = E_N + IR_t \quad (9)$$

Where, I is the current density and R_t is the total resistance at E_{appl} related to charge species transportation process. Therefore, E_N can be determined after I and R_t are measured at E_{appl} according to Eq. (9). It is important to recognize that E_N is a function of I, since the local gas compositions (and hence the local Nernst voltage) change as the current density changes due to local consumption/production of reactants/products at both the anode and the cathode. Alternatively, E_N can also be calculated theoretically according to the Nernst Eq. (10), if the detailed local gas composition, temperature and pressure in a reaction system are known.

$$E_N = -\frac{\Delta G(T)}{nF} \quad (10)$$

Where, n is the number of transferred electrons, F is the Faradaic constant and $\Delta G(T)$ is the Gibbs free energy. It should be noted that a reaction is spontaneous when the value of E_N is positive; in contrast, an applied voltage is required to drive a reaction when the value of E_N is negative. Therefore, from the perspective of thermodynamics, the E_N is solely dependent on state variables: temperature, gas compositions and pressure, which we refer to here as first-order factors. However, second-order factors such as electrode microstructure (porosity, diameter of the pores, electrode thickness, grain size), the effective diffusivities of CO and CO_2, and the gas flow rate will also influence the CO/CO_2 concentration distribution in practical SOECs. This means that the E_N will likely vary to a certain extent for SOECs with different electrode microstructures even when subjected to the same operating conditions, i.e. different E_N~E_{appl} relationships can be expected for different SOECs. While we recognize that these second-order factors can affect the first-order factor of local gas composition, these second-order factors do not adversely impact the central findings of this work—these kinetic effects will modify the boundaries for carbon deposition and Ni oxidation, but do not change the underlying thermodynamic principles that control the favorability of these processes. Thus, only the implications of the first-order factors of temperature, gas composition and pressure are discussed in this work.

In order to improve the applicability of the above thermodynamic model, assumptions used for the practical SOECs system are: (a) the reactions in SOECs during CO_2 electrolysis are in a steady state at E_{appl};

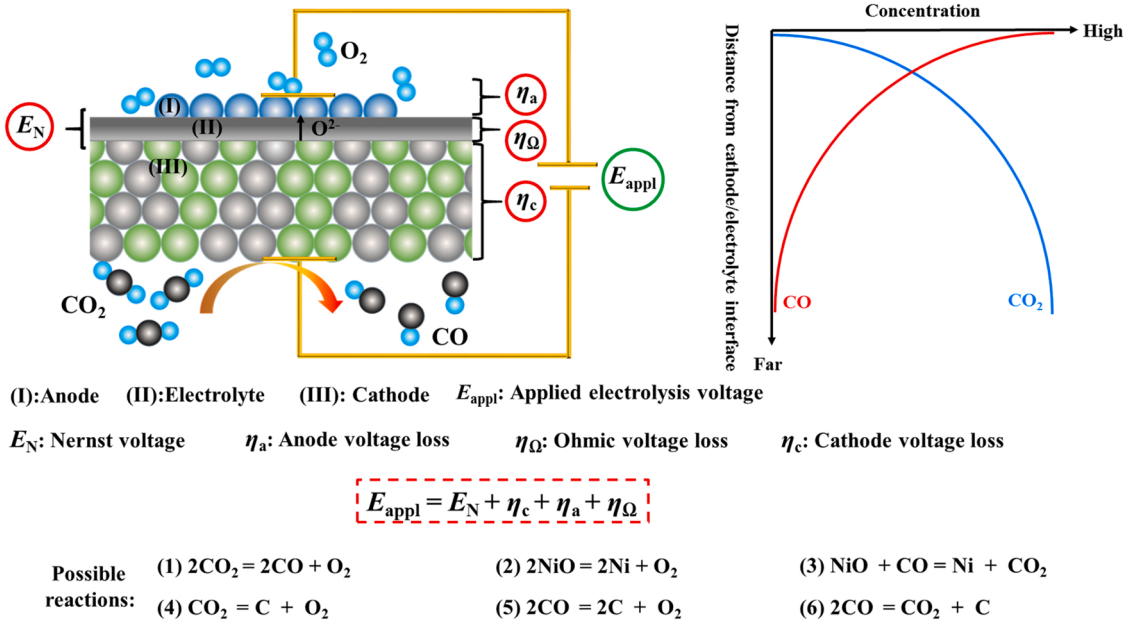

Fig. 1. Summary of possible reactions in SOEC-based CO_2 electrolysis and schematic illustration of the voltage distribution across a SOEC when an electrolysis voltage is applied. The applied electrolysis voltage (E_{appl}) counteracts not only the anode voltage loss (η_a), ohmic voltage loss (η_Ω) and cathode voltage loss (η_c), but also the Nernst voltage (E_N) determined by the local gas compositions on the cathode and anode side of the cell. Reaction (1) is the targeted CO_2 electrolysis reaction in this system; reactions (2) and (3) are two possible paths for NiO reduction; reactions (4)-(6) are three possible paths for carbon deposition. The inset on the right schematically illustrates the concentration gradients of CO_2 and CO across the cathode during electrolysis operation; CO_2 is depleted while the CO concentration is enriched close to the active cathode/electrolyte interface due to the respective consumption and production of these two species.

(b) the temperature is uniform across the electrodes; (c) the P_{O_2} at the anode is constant under different E_{appl} and always equals to 0.208 atm when air of 100 mL min^{-1} is used as anode sweep gas.

3.3. Theoretically rational E_N window at different temperature

A typical electrolysis operating condition entails CO_2 (with or without safe gas) and air (P_{O_2} = 0.208 atm) feeds to the cathode and anode respectively at 1 atm and 800 °C.[29,30] With increasing E_{appl} (and thus increasing current density), one can expect the proportion of CO in the cathode to increase as the CO_2 is reduced to CO and O^{2-}. The thermodynamic favorability of the undesired carbon deposition and Ni oxidation reactions will depend on the relative partial pressures of CO vs. CO_2 in the cathode and/or the partial pressure of O_2 in the anode. We can therefore use the Nernst equation to calculate the theoretical E_N of these undesired cathode reactions as a function of the CO partial pressure (P_{CO}) while fixing the oxygen partial pressure (P_{O_2}) at the anode at 0.208 atm (Fig. 2 **a-c**). The E_N of the desired CO_2 electrolysis reaction ((1): $2CO_2 \rightarrow 2CO + O_2$) decreases with increasing P_{CO}, intersecting the NiO electro-reduction reaction ((2): $NiO \rightarrow 2Ni + O_2$) at P_{CO} = 0.00514 atm, $E_N = -0.701$ V. At much higher CO pressures, E_N for CO_2 electrolysis then intersects with E_N for the electrochemical carbon deposition reactions ((4): $CO_2 \rightarrow C + O_2$ and (5): $2\,CO \rightarrow 2\,C + O_2$) at P_{CO} = 0.889 atm, $E_N = -1.040$ V (Fig. 2 **b**). While the E_N of NiO electro-reduction reaction ((2): $2NiO \rightarrow Ni + O_2$) does not depend on P_{CO}, and thus is constant (−0.701 V) in Fig. 2 **b**, it does depend on the anode-side P_{O_2} as shown in Fig. 2 **e**. It should be noted that the two thermochemical reactions ((3): $NiO + CO \rightarrow Ni + CO_2$ and (6): $2CO \rightarrow CO_2 + C$) will proceed spontaneously when P_{CO} is higher than 0.00514 atm and 0.889 atm, respectively (Fig. 2 **a** and **c**), as their E_N become positive (i.e. $\Delta G < 0$). This means NiO can be electro-reduced (i.e., Ni oxidation is suppressed) when E_N for the cell exceeds − 0.701 V while carbon deposition is promoted thermodynamically when E_N for the cell exceeds − 1.040 V. Therefore, a SOEC operational voltage window exists for pure CO_2 electrolysis at 800 °C between − 0.701 and − 1.040 V wherein both Ni oxidation and carbon deposition are thermodynamically inhibited. By extending this analysis to different temperatures (Fig. S3 and Table S1), a thermodynamic reaction phase diagram is obtained that specifies the safe operating voltage window for CO_2 electrolysis (Fig. 2 **d**). As shown in this diagram, E_N for NiO electro-reduction decreases with increasing temperature, while E_N for carbon deposition increases with increasing temperature, thus the safe operational voltage window broadens with increasing temperature, i.e., from ΔE = 0.153 V at 500 °C to ΔE = 0.514 V at 1000 °C.

In a practical application, it is important to achieve high CO_2 conversion. However, with increasing conversion of CO_2 to CO, a threshold CO concentration is eventually reached where carbon deposition becomes thermodynamically favored (Fig. S4). This threshold value increases with increasing temperature from 6.22% at 500 °C to 88.9% at 800 °C and further to 99.3% at 1000 °C, implying that carbon deposition is especially problematic at low temperatures. Therefore, CO_2 electrolysis at high temperature not only leads to faster kinetics, but also higher resistance to carbon deposition (as has been previously observed by many researchers), indicating that high-temperature (> 800 °C) SOEC operation is particularly desired for CO_2 electrolysis.

3.4. The effect of anode-side oxygen partial pressure on the rational E_N window

Beyond the CO/CO_2 composition at the cathode, the anode-side P_{O_2} ($P_{O_{2\ anode}}$) can also influence the stable SOEC operating voltage window. To examine this issue, we first fixed the gas composition at the cathode to the threshold value above which carbon deposition is favored at 800 °C (i.e., 88.91% CO - 11.09% CO_2, 1 atm). We then varied the $P_{O_{2\ anode}}$ from 10^{-20} to 10 atm. As shown in Fig. 2 **e**, the E_N's of all reactions decrease at the same rate with increasing $P_{O_{2\ anode}}$. Note that thermochemical reactions (3) and (6) are excluded here as their E_N does not depend on $P_{O_{2\ anode}}$. Because E_N's for NiO reduction and carbon

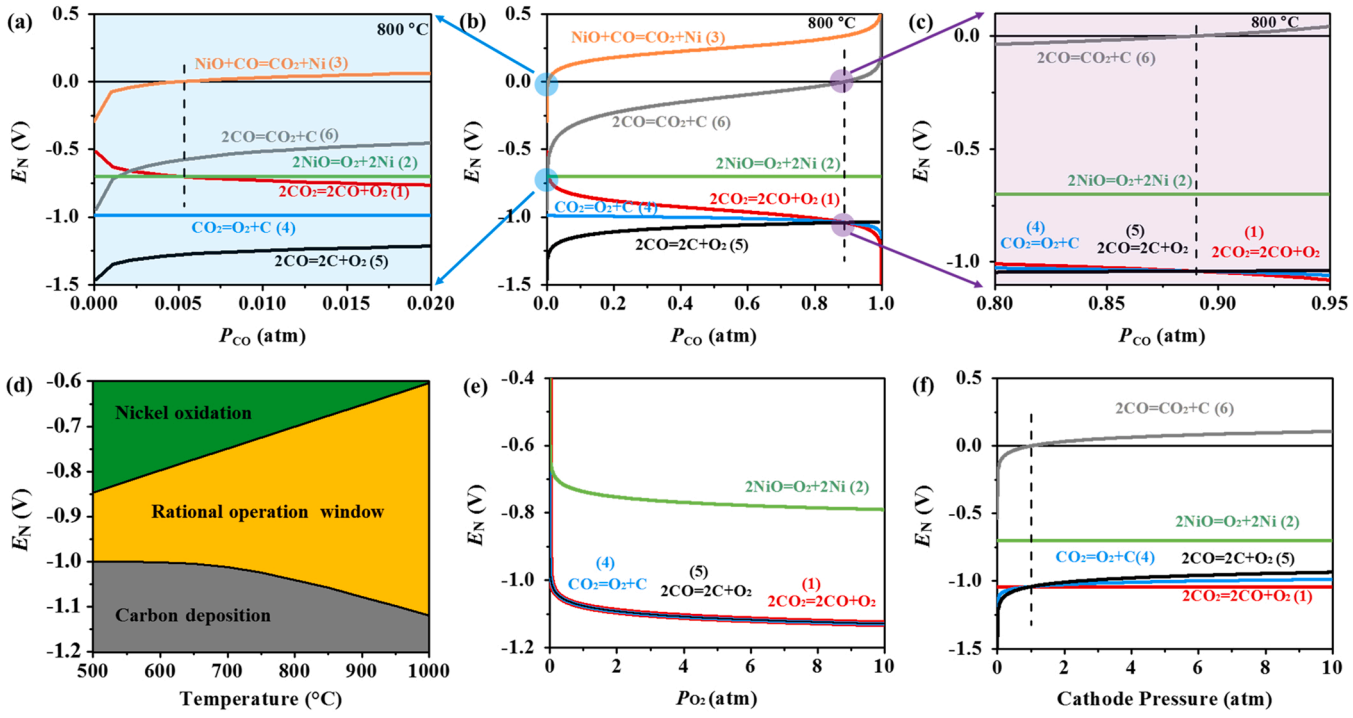

Fig. 2. Nernst equilibrium voltage (E_N) plotted against different conditions. (a) E_N vs. P_{CO} (at low values of P_{CO}), T = 800 °C, anode P_{O_2} = 0.208 atm; (b) E_N vs. P_{CO}, T = 800 °C, anode P_{O_2} = 0.208 atm; (c) E_N vs. P_{CO} (at high values of P_{CO}), T = 800 °C, anode P_{O_2} = 0.208 atm; (d) thermodynamic reaction phase diagram vs. T with anodeP_{O_2} = 0.208 atm, cathode total gas pressure = 1 atm; (e) E_N vs. anode P_{O_2} with cathode total gas pressure = 1 atm and cathode gas composition 88.91% CO - 11.09% CO_2, T = 800 °C; (f) E_N vs. total cathode gas pressure with composition 88.91% CO - 11.09% CO_2, T = 800 °C.

deposition both decrease at the same rate with increasing $P_{O_2\ anode}$, the width of the operational voltage window remains constant (Fig. S5), although the boundaries of the window shift to more negative absolute E_N values. This result demonstrates that high $P_{O_2\ anode}$ can enable stable SOEC operation (i.e., no carbon deposition) at higher applied voltages, as a higher E_N can be sustained before carbon deposition becomes favorable. Care should be taken, however, to ensure that the cell voltage remains high enough to avoid Ni oxidation.

3.5. The effect of cathode-side pressure on the rational E_N window

In addition, we also investigated the effect of cathode pressure on E_N by fixing the $P_{O_2\ anode}$ to 0.208 atm, while the cathode atmosphere composition was set at 88.91% CO - 11.09% CO_2 and the cathode atmosphere pressure was varied from 10^{-5} atm to 10 atm. Under these conditions, the E_N's for CO_2 electrolysis (reaction 1), and NiO electro-reduction, (reaction 2), are not affected while the E_N's of the carbon deposition reactions (reactions 4–6) increase with increasing total cathode gas pressure (Fig. 2**f**). When the cathode gas pressure is higher than 1 atm, the E_N of thermochemical carbon deposition (reaction 6), is positive while the E_N's of the electrochemical carbon deposition reactions are higher (less negative) than that of CO_2 electrolysis, revealing that higher cathode gas pressures will favor carbon deposition, while decreasing the cathode gas pressure will inhibit carbon deposition.

3.6. The effect of water vapor in the cathode on the rational E_N window

While the preceding analysis has been conducted under the assumption of 100% pure, dry cathode CO_2 flow, in practical applications the CO_2 feed stream will inevitably contain at least trace quantities of water vapor. In fact, H_2O is often co-fed with CO_2 to enable CO_2/H_2O co-electrolysis for syngas production. Additionally, the existence of H_2O has been experimentally proved to decrease the probability of carbon deposition, which is generally ascribed to the activation of the water-gas-shift-reaction. Thus, we used our thermodynamic approach to investigate the effect of cathode-feed water partial pressure ($P_{H_2O\ cathode}$) on the rational E_N boundaries for stable SOEC operation at 800 °C (Fig. S6). At 800 °C and $P_{O_2\ anode} = 0.208$ atm, the E_N of the NiO electro-reduction (reaction 2) remains constant at − 0.701 V, as this reaction equilibrium does not depend on the cathode gas species (CO_2 vs H_2O). Thus, we conclude that E_N for NiO electro-reduction is not affected by H_2O. Meanwhile, the E_N's for the carbon deposition reactions (reaction 4, 5 and 6), are controlled by $P_{O_2\ anode}$, P_{CO_2} and P_{CO}. While the total combined pressure of CO_2 and CO at cathode side cannot be altered by the P_{H_2O}, the ratio between them can be altered as H_2O activates the water gas shift reaction (WGS).[31,32] This necessarily results in a decrease in the CO partial pressure and an increase in the CO_2 partial pressure relative to the case for the dry CO_2/CO equilibrium which pushes the E_N's for the carbon deposition reactions to more negative values and increases the safe voltage window for coke-free SOEC operation. To quantify this effect, we calculated the E_N's of carbon deposition and CO_2 conversion boundaries for different cathode feed compositions (1-x) atm CO_2 - x atm H_2O ($0 \leq x \leq 0.8$, Fig. S6). Table S2 provides the equilibrium gas partial pressures at the threshold value for carbon deposition. Here, we take two cases (0.99 atm CO_2-0.01 atm H_2O and 0.8 atm CO_2-0.2 atm H_2O) as examples to demonstrate the identification of E_N for carbon deposition (Fig. S6 **a** and **b**). The E_N of carbon deposition decreases (becomes more negative) with increasing P_{H_2O}, varying from − 1.040 V to − 1.111 V as P_{H_2O} increases from 0 atm to 0.8 atm. Meanwhile, we also calculated the CO_2 conversion boundaries for CO_2/H_2O co-electrolysis (Fig. S6 **d**). The results clearly show that increasing P_{H_2O} can improve the CO_2 conversion boundary for safe operation, which theoretically increases from 88.91% to 97.34% with P_{H_2O} increasing from 0 atm to 0.8 atm.

Based on the preceding analyses, we can conclude that high temperature, low cathode pressure (and/or reduced cathode CO partial pressure via addition of H_2O, N_2 etc.) and high anode P_{O_2} suppress carbon deposition, while high temperature and low anode P_{O_2} suppress Ni oxidation. These results further confirm that a rational operating window exists where both carbon deposition and Ni oxidation are thermodynamically suppressed under realistic temperature, pressure, and cell voltage conditions for CO_2 electrolysis in Ni-SOECs.

3.7. The relationship between E_N and E_{appl} in practical SOECs

To confirm the validity of this "safe" operational window in a practical application, we experimentally investigated CO_2 electrolysis with lab-scale Ni/YSZ-based SOEC button cells under a variety of conditions. We chose a typical reaction condition (cathode: CO_2 1 atm, anode: air 1 atm; temperature: 800 °C) for CO_2 electrolysis. Under these conditions, the theoretically calculated operational window is (−0.701 V to −1.040 V). In order to examine the lower voltage boundary associated with NiO reduction, we first carried out CO_2 electrolysis on two Ni-SOECs that had not been pre-reduced with H_2 gas, and thus contained NiO rather than Ni metal in the cathode. Both cells showed an onset in electrochemical activity at ~ − 0.822 V (Fig. S7), suggesting that this voltage represents the boundary for the onset of NiO electro-reduction. This voltage is more negative than the thermodynamically calculated value of − 0.701 V (by ~ 120 mV), presumably because an additional voltage loss (E_{loss}) must be overcome to activate the electro-reduction process.

We subsequently fully reduced a cell under flowing H_2 and then performed additional CO_2 electrolysis testing. After H_2 reduction, the cell's open circuit voltage (OCV) under CO_2/air feed reaches 0.705 V (Fig. 3 **a**). According to the working principle of solid oxide cells, OCV is a function of the P_{O_2} difference between anode and cathode. In this case, the OCV should reflect the reaction equilibrium between CO_2 ($2CO_2 \rightarrow 2CO + O_2$) and Ni oxidation ($Ni + CO_2 \rightarrow NiO + CO$) on the cathode (see Section 2 in SI). Therefore, the OCV can be considered as an electrochemical indicator to judge whether NiO is reduced to Ni or not. The value of 0.705 V obtained here indicates that the NiO to Ni reduction process is completed.

Our Ni/YSZ-based SOEC shows high activity towards pure CO_2 electrolysis, reaching a current density of − 1.212 A cm^{-2} at − 1.6 V (Fig. 3**b**), which is comparable to recent results reported by other groups.[15,29] CO_2 starvation/mass transport issues are observed at high E_{appl} as indicated by the first-order derivative of the polarization curve (inset in Fig. 3**b**), where dE_{appl}/dI reaches the maximum value at − 1.384 V.

To reveal the relationship between E_N and E_{appl}, polarization curves and electrochemical impedance spectra (EIS) at different E_{appl} were measured repeatedly (Fig. S8-S14). According to equation (9), E_N at different E_{appl} were then calculated (Fig. 3**c**). E_N falls into the safe operational window when E_{appl} is between − 0.9 V and − 1.2 V. This means the cell is susceptible to Ni oxidation if E_{appl} falls below − 0.9 V, while carbon deposition may occur if E_{appl} exceeds − 1.3 V. According to the working principle of SOECs, the E_N should increase with increasing E_{appl}. The lower value of E_N at − 1.5 V is caused by the emergence of gas concentration polarization (a non-charged species transportation process) when E_{appl} exceeds − 1.384 V, as shown in Fig. 3**b**. The value of R_t in Eq. (9) increases with E_{appl} due to the gas concentration polarization resistance, which leads to a lower E_N. We confirm the validity of the lower boundary by potentiostatic testing at − 0.8 V (Fig. S15), showing that NiO cannot be electro-reduced at this condition.

3.8. Characterizations of Ni-SOECs

As shown in Fig. 4 **a**, stable SOEC operation is confirmed at the lower "safe" boundary of − 0.9 V. After a rapid initial increase to − 60 mA cm^{-2} during the first 20 min, the current density gradually decreases and

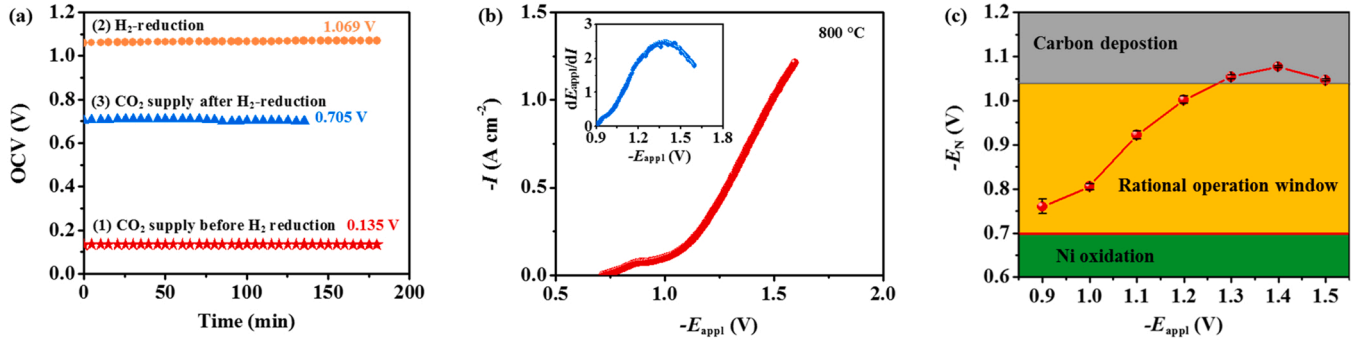

Fig. 3. Electrochemical characterization at 800 °C of Ni-SOECs after H_2 reduction. (a) Open circuit voltage (OCV) under different conditions, (b) polarization curve and its first-order derivative (inset) for pure CO_2 electrolysis and (c) the calculated E_N with error bars at different E_{appl}.

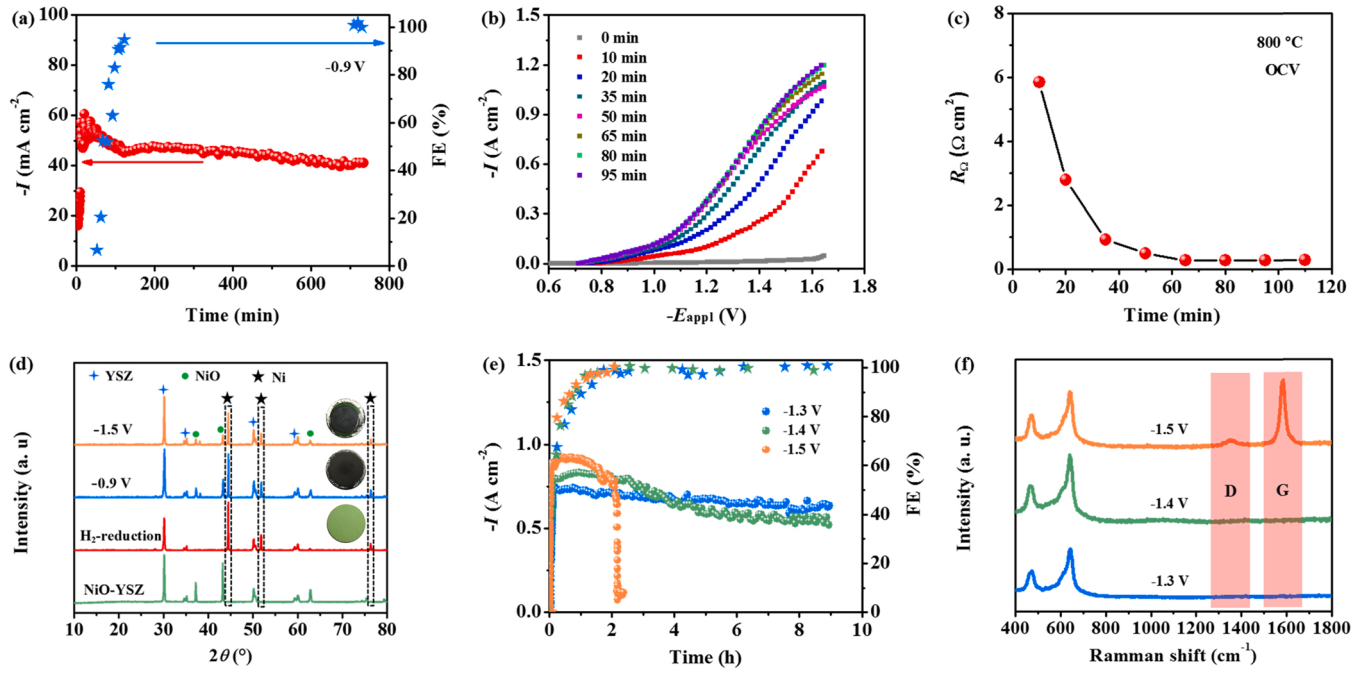

Fig. 4. Electrochemical behavior and characterization of NiO-YSZ cathode at 800 °C for pure CO_2 electrolysis. (a) Potentiostatic testing at − 0.9 V with Faradaic efficiency (FE), (b) polarization curves at different time intervals during the − 0.9 V potentiostatic testing, (c) ohmic resistance (R_Ω) variation during the − 0.9 V potentiostatic testing, (d) X-ray diffraction patterns of unreduced NiO-YSZ cathode, H_2-reduced cathode, and cathodes that were electro-reduced at − 0.9 V and − 1.5 V (digital photos in insets), (e) potentiostatic testing and FE's at − 1.3 V, − 1.4 V and − 1.5 V, (f) Raman spectra of NiO-YSZ after potentiostatic testing at − 1.3 V, − 1.4 V and − 1.5 V with the Raman shift windows for the D and G bands of carbon highlighted.

then stabilizes. The Faradaic efficiency (FE) holds close to 0 during the first 50 min, suggesting remnant NiO is being reduced to Ni during this incubation period, before rapidly increasing above 90% over the following 57 min, and then stabilizing at close to 100% for the remainder of the potentiostatic testing. The polarization behavior (Fig. 4 **b**) and ohmic resistance (R_Ω, Fig. 4 **c**) trends are consistent with this interpretation, showing a rapid improvement in performance commensurate with a rapid decrease in the cell ohmic resistance over the first 50–60 min of testing prior to stabilization. We tested a second cell under identical conditions with similar results (Fig. S16). In this second test, we subsequently withdrew the − 0.9 V driving voltage and continuously monitored the OCV while continuing to supply CO_2 and air to the cell. The cell maintained the OCV of ~0.705 V for 60 min before rapidly decreasing thereafter. Collectively, the results from these two cells imply: 1) that NiO is electro-reduced under a driving voltage of − 0.9 V, 2) Ni metal remains reduced at − 0.9 V, and 3) Ni re-oxidation occurs under OCV conditions at a voltage of 0.705 V. All conclusions are consistent with the results of Fig. 3 **c**. To further confirm these conclusions, we acquired XRD patterns for the NiO-YSZ cathodes before and after these electrochemical investigations (Fig. 4 **d**). The clear presence of Ni diffraction peaks and the visual color change of the cathode from green (NiO) to black (Ni) demonstrate that NiO is electro-reduced to Ni metal by potentiostatic operation at − 0.9 V. The existence of remnant NiO diffraction peaks in these tests is ascribed to two factors: a) discontinuous (non-percolating) NiO or NiO that is encapsulated by the YSZ phase, which thus cannot be electro-reduced and b) remnant unreduced interior regions of the NiO phase. Scanning electron microscopy (SEM) imaging and elemental mapping provide further confirmation that NiO is electro-reduced at − 0.9 V (Fig. 5 **a-e**).

Turning now to the upper safe voltage boundary, we examine electrochemical behavior with potentiostatic testing at E_{appl} values of − 1.3, − 1.4, and − 1.5 V, respectively. In all cases, the current density increases sharply with FE increasing close to 100% in the first 2 h (Fig. 4 **e**). For the cells tested at − 1.3 V and − 1.4 V, the cell current density then begins to gradually decrease. For the cell tested at − 1.5 V, however, the cell current density drops sharply, implying carbon deposition

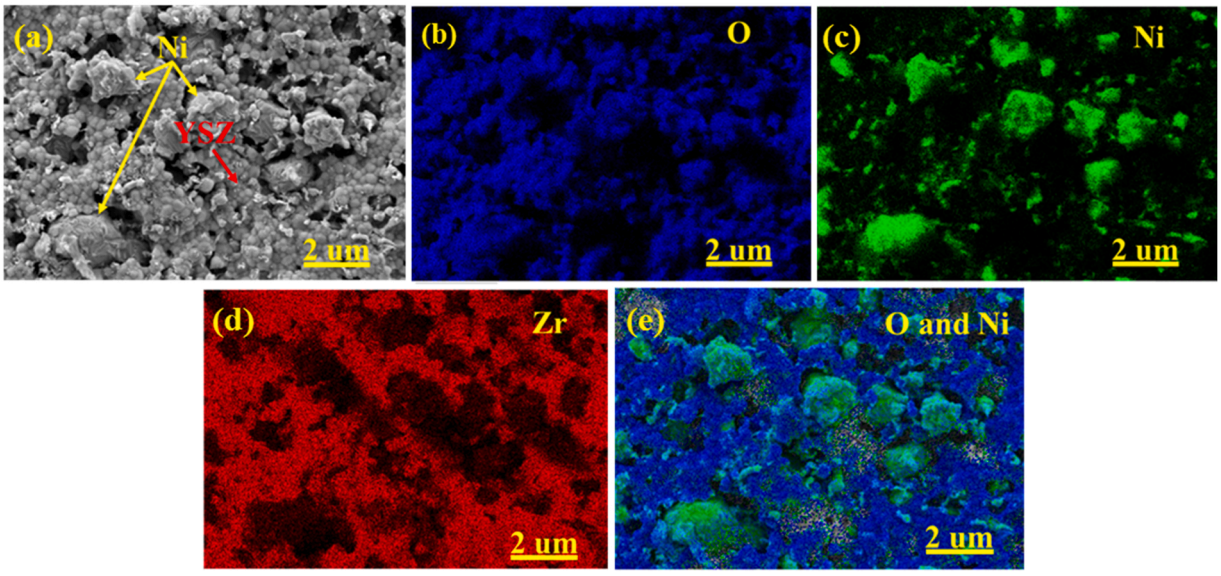

Fig. 5. Microstructure characterization of NiO-YSZ cathode after − 0.9 V potentiostatic testing at 800 °C. (a) Top-view scanning electron microscopy image, (b) O mapping, (c) Ni mapping, (d) Zr mapping and (e) overlapped O and Ni mapping.

likely occurs at − 1.5 V. According to Fig. 3 **c**, any $E_{appl} \leq -1.3$ V should fall within the carbon deposition area, however we only detect a clear Raman signal from carbon species (carbon D and G bands between 1300 cm^{-1} and 1600 cm^{-1}) after the testing at − 1.5 V (Fig. 4**f**). A carbon signal was also observed in the porous structure of the Ni-YSZ cathode close to the YSZ electrolyte after the − 1.5 V testing (Fig. S17). We attribute the higher experimentally observed voltage onset for carbon deposition relative to the thermodynamic prediction to the fact that the locally increased P_{O_2} at anode/electrolyte interface due to gas transport limitations thermodynamically suppresses carbon deposition (Fig. 2 **e**). For simplification, our thermodynamic analysis was established based on the assumption that the P_{O_2} at anode is constant at 0.208 atm (air). However, the P_{O_2} (or at least the effective O_2 chemical potential) at anode/electrolyte interface can reach even to 100 atm during operation at high current densities, since O_2 is produced at the anode/electrolyte interface.[33] Such a high $P_{O_{2\ anode}}$ would cause the E_N threshold for carbon deposition to shift from − 1.040 V to − 1.183 V, thereby elevating the minimum applied voltage required for carbon deposition.

3.9. Stability test of Ni-SOECs

It is interesting to note that the current density at − 1.5 V recovers as time elapses (Fig. 6 **a**), implying that the deposited carbon can be eliminated via the reverse of reaction (6). The phenomenon is attributed to electrochemical performance degradation caused by microstructural changes in the SOEC electrode. Since carbon deposition is caused by a high local P_{CO} at cathode active sites, performance degradation leads to a reduction in CO production (and hence a reduction in P_{CO}) and thus reduces the risk of carbon deposition and/or can even cause it to partially reverse. Longer term testing (Fig. 6 **b**) above the carbon deposition voltage threshold leads to irreversible electrochemical performance degradation caused by microstructure changes, as is widely reported by other groups.[24,34,35] Severe Ni depletion and coarsening is found in the Ni-YSZ cathode after potentiostatic testing for 250 h at − 1.5 V (Fig. S18), reflected by a commensurate increase in R_Ω from 0.199 Ω cm^2 to 0.353 Ω cm^2 (Fig. S19). This phenomenon is commonly considered to be related with the surface Gibbs energy of metal Ni or the wettability of Ni on YSZ surface, which are closely affected by the oxygen and/or steam partial pressure.[36-38] The Ni depletion near the cathode/electrolyte interface shifts the TPBs outwards and increases the thickness of electrolyte, thus increases R_Ω. The Ni coarsening destroys the originally percolated Ni phase (electron conduction path) and generates isolated Ni islands which are susceptible to re-oxidation, thus reducing the electric conductivity of cathode and causing an increase in

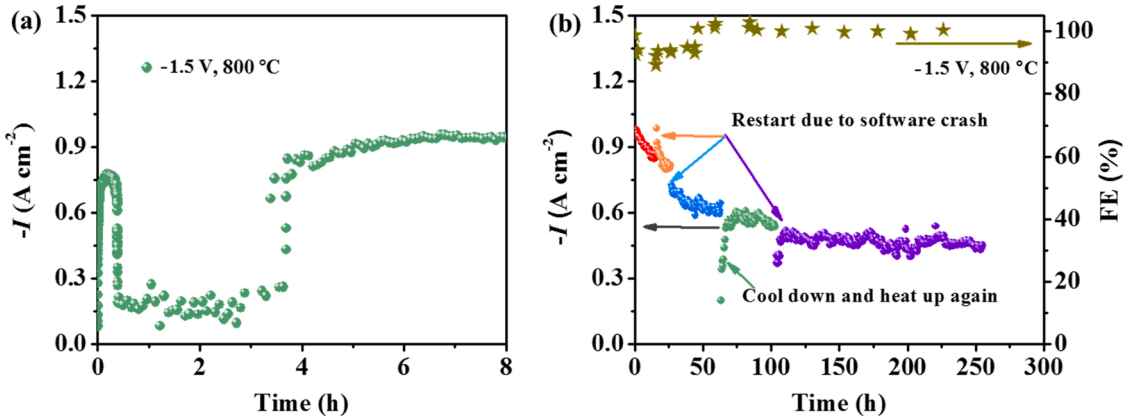

Fig. 6. Repeated performance measurement of NiO-YSZ based SOECs for pure CO_2 electrolysis at 800 °C and − 1.5 V. (a) Initial stage (< 10 h) and (b) long term testing for more than 250 h.

R_Ω. In addition, the reaction polarization resistance (extracted from the high frequency impedance arc), which is related to the charge transfer at the Ni-YSZ cathode/electrolyte interface,[39-41] increases from 0.098 Ω cm^2 to 0.180 Ω cm^2 due to the decrease in TPBs density as the microstructure coarsens. Meanwhile, the transport polarization resistance (extracted from the low frequency impedance arc), which is related to gas diffusion and conversion processes,[42-44] slightly decreases from 0.265 Ω cm^2 to 0.231 Ω cm^2 after potentiostatic testing, probably because the coarsening microstructure facilitates CO_2 diffusion. Therefore, exploring the degradation mechanisms of Ni-based cathode and developing stability improvement strategies are the first priority to be considered in the future works to accelerate the application of Ni-SOECs for CO_2 electrolysis.

4. Conclusion

This work provides thermodynamic insights into the origin of Ni oxidation and carbon deposition during CO_2 electrolysis in Ni-based SOECs. The Nernst voltage (E_N) that develops across the SOEC, in relation to the driving voltage applied to the SOEC (E_{appl}) is the determining factor in controlling Ni oxidation and carbon deposition. Based on this principle, a thermodynamic reaction phase diagram can be established that effectively predicts the safe operational window for CO_2 electrolysis under different conditions. Experimentally, we confirm that both Ni oxidation and carbon deposition can be simultaneously inhibited in the electrolysis voltage window from − 0.9 V to − 1.4 V under typical CO_2 electrolysis conditions (cathode: CO_2 1 atm, anode: air 1 atm, temperature: 800 °C). However, Ni-based SOECs still demonstrate performance degradation due to Ni coarsening and depletion under these operation conditions, thus future research should be focused on exploring the mechanism of Ni coarsening and depletion, as well as developing methods and materials to inhibit Ni coarsening and depletion.

CRediT authorship contribution statement

Shiqing Hu: Conceptualization, Methodology, Validation, Investigation, Writing – original draft. **Bingjie Pang:** Date curation. **Liming Zhang:** Investigation. **Zhongwei Cao:** Investigation. **Peng Zhang:** Funding acquisition. **Yunjie Ding:** Supervision. **Ryan O'Hayre:** Writing – review & editing, Formal analysis. **Xuefeng Zhu:** Conceptualization, Writing – review & editing, Funding acquisition. **Weishen Yang:** Supervision.

Declaration of Competing Interest

The authors declare that they have no known competing financial interests or personal relationships that could have appeared to influence the work reported in this paper.

Data Availability

Data will be made available on request.

Acknowledgement

We thank for the financial support from National Key R&D Program of China (2022YFB3805501), National Natural Science Foundation of China (No. 22178332) and DICP (DICP I202221).

Appendix A. Supporting information

Supplementary data associated with this article can be found in the online version at doi:10.1016/j.apcatb.2022.122239.

References

[1] P. Vaziri, A review of the use of renewable energy in industry to reduce pollution, Chem. Method. 6 (2022) 174–183, https://doi.org/10.22034/chemm.2022.322945.1418.
[2] S. Chu, A. Majumdar, Opportunities and challenges for a sustainable energy future, Nature 488 (2012) 294–303, https://doi.org/10.1038/nature11475.
[3] D.H. Vo, A.T. Vo, C.M. Ho, H.M. Nguyen, The role of renewable energy, alternative and nuclear energy in mitigating carbon emissions in the CPTPP countries, Renew. Energ. 161 (2020) 278–292, https://doi.org/10.1016/j.renene.2020.07.093.
[4] A. Ozden, F.P. Garcia de Arquer, J.E. Huang, J. Wicks, J. Sisler, R.K. Miao, C. P. O'Brien, G. Lee, X. Wang, A.H. Ip, E.H. Sargent, D. Sinton, Carbon-efficient carbon dioxide electrolysers, Nat. Sustain 5 (2022) 563–573, https://doi.org/10.1038/s41893-022-00879-8.
[5] R. Xia, S. Overa, F. Jiao, Emerging electrochemical processes to decarbonize the chemical industry, JACS Au 2 (2022) 1054–1070, https://doi.org/10.1021/jacsau.2c00138.
[6] H. Seo, M. Rahimi, T.A. Hatton, Electrochemical carbon dioxide capture and release with a redox-active amine, J. Am. Chem. Soc. 144 (2022) 2164–2170, https://doi.org/10.1021/jacs.1c10656.
[7] A. Hauch, R. Kungas, P. Blennow, A.B. Hansen, J.B. Hansen, B.V. Mathiesen, M. B. Mogensen, Recent advances in solid oxide cell technology for electrolysis, eaba6118, Science 370 (2020), https://doi.org/10.1126/science.aba6118.
[8] S.D. Ebbesen, M. Mogensen, Exceptional durability of solid oxide cells, Electrochem. Solid-State Lett. 13 (2010) B106–B108, https://doi.org/10.1149/1.3455882.
[9] L. Lu, W. Liu, J. Wang, Y. Wang, C. Xia, X.-D. Zhou, M. Chen, W. Guan, Long-term stability of carbon dioxide electrolysis in a large-scale flat-tube solid oxide electrolysis cell based on double-sided air electrodes, Appl. Energy 259 (2020), 114130, https://doi.org/10.1016/j.apenergy.2019.114130.
[10] Y. Tao, S.D. Ebbesen, M.B. Mogensen, Degradation of solid oxide cells during co-electrolysis of steam and carbon dioxide at high current densities, J. Power Sources 328 (2016) 452–462, https://doi.org/10.1016/j.jpowsour.2016.08.055.
[11] J. Carneiro J, X.-K. Gu, E. Tezel, E. Nikolla, Electrochemical reduction of CO_2 on metal-based cathode electrocatalysts of solid oxide electrolysis cells, Ind. Eng. Chem. Res. 59 (2020) 15884–15893, https://doi.org/10.1021/acs.iecr.0c02773.
[12] D. Chen, D.K. Niakolas, V. Papaefthimiou, E. Ioannidou, S.G. Neophytides, S. Zafeiratos, How the surface state of nickel/gadolinium-doped ceria cathodes influences the electrochemical performance in direct CO_2 electrolysis, J. Catal. 404 (2021) 518–528, https://doi.org/10.1016/j.jcat.2021.10.027.
[13] B.N. Nguyen, N.K. Karri, C.J.T. Mason, J.F. Fitzpatrick, B.J. Koeppel, Damage modeling of solid oxide fuel cells accounting for redox effects, J. Electrochem. Soc. 168 (2021), 114514, https://doi.org/10.1149/1945-7111/ac39de.
[14] Y. Ishibashi, K. Matsumoto, S. Futamura, Y. Tachikawa, J. Matsuda, S.M. Lyth, Y. Shiratori, S. Taniguchi, K. Sasaki, Improved redox cycling durability in alternative Ni alloy-based SOFC anodes, J. Electrochem. Soc. 167 (2020), 124517, https://doi.org/10.1149/1945-7111/abac87.
[15] Y. Song Y, Z. Zhou, X. Zhang, Y. Zhou, H. Gong, H. Lv, Q. Liu, G. Wang, X. Bao, Pure CO_2 electrolysis over an Ni/YSZ cathode in a solid oxide electrolysis cell, J. Mater. Chem. A 6 (2018) 13661–13667, https://doi.org/10.1039/C8TA02858C.
[16] V. Duboviks, R.C. Maher, M. Kishimoto, L.F. Cohen, N.P. Brandon, G.J. Offer, A raman spectroscopic study of the carbon deposition mechanism on Ni/CGO electrodes during CO/CO_2 electrolysis, Phys. Chem. Chem. Phys. 16 (2014) 13063–13068, https://doi.org/10.1039/C4CP01503G.
[17] T.L. Skafte, Z. Guan, M.L. Machala, C.B. Gopal, M. Monti, L. Martinez, E. Stamate, S. Sanna, J.A. Garrido Torres, E.J. Crumlin, M. García-Melchor, M. Bajdich, W. C. Chueh, C. Graves, Selective high-temperature CO_2 electrolysis enabled by oxidized carbon intermediates, Nat. Energy 4 (2019) 846–855, https://doi.org/10.1038/s41560-019-0457-4.
[18] F. Yu, J. Xiao, Y. Zhang, W. Cai, Y. Xie, N. Yang, J. Liu, M. Liu, New insights into carbon deposition mechanism of nickel/yttrium-stabilized zirconia cermet from methane by in situ investigation, Appl. Energy 256 (2019), 113910, https://doi.org/10.1016/j.apenergy.2019.113910.
[19] V. Duboviks, M. Lomberg, R.C. Maher, L.F. Cohen, N.P. Brandon, G.J. Offer, Carbon deposition behaviour in metal-infiltrated gadolinia doped ceria electrodes for simulated biogas upgrading in solid oxide electrolysis cells, J. Power Sources 293 (2015) 912–921, https://doi.org/10.1016/j.jpowsour.2015.06.003.
[20] J.T.S. Irvine, D. Neagu, M.C. Verbraeken, C. Chatzichristodoulou, C. Graves, M. B. Mogensen, Evolution of the electrochemical interface in high-temperature fuel cells and electrolysers, Nat. Energy 1 (2016) 15014, https://doi.org/10.1038/nenergy.2015.14.
[21] D. Neagu, T.S. Oh, D.N. Miller, H. Menard, S.M. Bukhari, S.R. Gamble, R.J. Gorte, J.M. Vohs, J.T. Irvine, Nano-socketed nickel particles with enhanced coking resistance grown in situ by redox exsolution, Nat. Commun. 6 (2015) 8120, https://doi.org/10.1038/ncomms9120.
[22] W. Yue, Y. Li, Y. Zheng, T. Wu, C. Zhao, J. Zhao, G. Geng, W. Zhang, J. Chen, J. Zhu, B. Yu, Enhancing coking resistance of Ni/YSZ electrodes: In situ characterization, mechanism research, and surface engineering, Nano Energy 62 (2019) 64–78, https://doi.org/10.1016/j.nanoen.2019.05.006.
[23] A.K. Opitz, A. Nenning, C. Rameshan, M. Kubicek, T. Gotsch, R. Blume, M. Havecker, A. Knop-Gericke, G. Rupprechter, B. Klotzer, J. Fleig, Surface chemistry of perovskite-type electrodes during high temperature CO_2 electrolysis investigated by operando photoelectron spectroscopy, ACS Appl. Mater. Interfaces 9 (2017) 35847–35860, https://doi.org/10.1021/acsami.7b10673.

[24] Y. Tao, S.D. Ebbesen, M.B. Mogensen, Carbon deposition in solid oxide cells during co-electrolysis of H_2O and CO_2, F337-F343, J. Electrochem. Soc. 163 (2014), https://doi.org/10.1149/2.079403jes.
[25] J. Wang, S.R. Bishop, L. Sun, Q. Lu, G. Vardar, R. Bliem, N. Tsvetkov, E.J. Crumlin, J.-J. Gallet, F. Bournel, I. Waluyo, B. Yildiz, Threshold catalytic onset of carbon formation on CeO_2 during CO_2 electrolysis: mechanism and inhibition, J. Mater. Chem. A 7 (2019) 15233–15243, https://doi.org/10.1039/C9TA03265G.
[26] Y. Shi, Y. Luo, N. Cai, J. Qian, S. Wang, W. Li, H. Wang, Experimental characterization and modeling of the electrochemical reduction of CO_2 in solid oxide electrolysis cells, Electrochim. Acta 88 (2013) 644–653, https://doi.org/10.1016/j.electacta.2012.10.107.
[27] H. Xu, J. Ma, P. Tan, Z. Wu, Y. Zhang, M. Ni, J. Xuan, Enabling thermal-neutral electrolysis for CO_2-to-fuel conversions with a hybrid deep learning strategy, Energy Convers. Manag. 230 (2021), 113827, https://doi.org/10.1016/j.enconman.2021.113827.
[28] M. Ni, Modeling of a solid oxide electrolysis cell for carbon dioxide electrolysis, Chem. Eng. J. 164 (2010) 246–254, https://doi.org/10.1016/j.cej.2010.08.032.
[29] L. Sun, Q. Zheng, N. Li, C. Chen, Z. Zhan, Direct electrolysis of CO_2 in solid oxide cells supported on ceramic fuel electrodes with straight open pores and coated catalysts, Solid State Ion. 344 (2020), 115154, https://doi.org/10.1016/j.ssi.2019.115154.
[30] H. Lv, L. Lin, X. Zhang, R. Li, Y. Song, H. Matsumoto, N. Ta, C. Zeng, Q. Fu, G. Wang, X. Bao, Promoting exsolution of RuFe alloy nanoparticles on $Sr_2Fe_{1.4}Ru_{0.1}Mo_{0.5}O_{6-\delta}$ via repeated redox manipulations for CO_2 electrolysis, Nat. Commun. 12 (2021) 5665, https://doi.org/10.1038/s41467-021-26001-8.
[31] E. Ioannidou, M. Chavani, S.G. Neophytides, D.K. Niakolas, Effect of the PH_2O-PCO_2 and PH_2 on the intrinsic electro-catalytic interactions and the CO production pathway on Ni-GDC during solid oxide H_2O-CO_2 co-electrolysis, J. Catal. 404 (2021) 174–186, https://doi.org/10.1016/j.jcat.2021.09.024.
[32] V. Kyriakou, D. Neagu, G. Zafeiropoulos, R.K. Sharma, C. Tang, K. Kousi, I. S. Metcalfe, van M.C.M. de Sanden, M.N. Tsampas, Symmetrical exsolution of Rh nanoparticles in solid oxide cells for efficient syngas production from greenhouse gases, ACS Catal. 10 (2019) 1278–1288, https://doi.org/10.1021/acscatal.9b04424.
[33] C. Graves, S.D. Ebbesen, S.H. Jensen, S.B. Simonsen, M.B. Mogensen, Eliminating degradation in solid oxide electrochemical cells by reversible operation, Nat. Mater. 14 (2015) 239–244, https://doi.org/10.1038/nmat4165.
[34] Y. Wang, C. Wu, B. Zu, M. Han, Q. Du, M. Ni, K. Jiao, Ni migration of Ni-YSZ electrode in solid oxide electrolysis cell: An integrated model study, J. Power Sources 516 (2021), 230660, https://doi.org/10.1016/j.jpowsour.2021.230660.
[35] M. Chen, Y.-L. Liu, J.J. Bentzen, W. Zhang, X. Sun, A. Hauch, Y. Tao, J.R. Bowen, P. V. Hendriksen, Microstructural degradation of Ni/YSZ electrodes in solid oxide electrolysis cells under high current, J. Electrochem. Soc. 160 (2013) F883–F891, https://doi.org/10.1149/2.098308jes.
[36] Y. Wang, C. Wu, B. Zu, M. Han, Q. Du, M. Ni, K. Jiao, Ni migration of Ni-YSZ electrode in solid oxide electrolysis cell: An integrated model study, J. Power Sources 516 (2021), 230660, https://doi.org/10.1016/j.jpowsour.2021.230660.
[37] W. Zhang, M. Chen, L. Theil Kuhn, J.R. Bowen, J.J. Bentzen, Electrochemistry unlocks wettability: Epitaxial growth of oxide nanoparticles on rough metallic surfaces, ChemElectroChem 1 (2014) 520–523, https://doi.org/10.1002/celc.201300045.
[38] Z. Jiao, N. Shikazono, Study on the effects of polarization on local morphological change of nickel at active three-phase-boundary using patterned nickel-film electrode in solid oxide fuel cell anode, Acta Mater. 135 (2017) 124–131, https://doi.org/10.1016/j.actamat.2017.05.051.
[39] Z. Huang, H. Qi, Z. Zhao, L. Shang, B. Tu, M. Cheng, Efficient CO_2 electroreduction on a solid oxide electrolysis cell with $La_{0.6}Sr_{0.4}Co_{0.2}Fe_{0.8}O_{3-\delta}$-$Gd_{0.2}Ce_{0.8}O_{2-\delta}$ infiltrated electrode, J. Power Sources 434 (2019), 226730, https://doi.org/10.1016/j.jpowsour.2019.226730.
[40] T. Su, Y. Li, S. Xue, Z. Xu, M. Zheng, C. Xia, Kinetics of CO_2 electrolysis on composite electrodes consisting of Cu and samaria-doped ceria, J. Mater. Chem. A 7 (2019) 1598–1606, https://doi.org/10.1039/C8TA09015G.
[41] S. Hu, L. Zhang, L. Cai, Z. Cao, Q. Jiang, W. Yu, Y. Wu, X. Zhu, W. Yang, Iron stabilized 1/3 A-site deficient La-Ti-O perovskite cathodes for efficient CO_2 electroreduction, J. Mater. Chem. A 8 (2020) 21053–21061, https://doi.org/10.1039/D0TA08088H.
[42] S.D. Ebbesen, M. Mogensen, Kinetics of oxidation of H_2 and reduction of H_2O in Ni-YSZ based solid oxide cells, ECS Trans. 50 (2013) 167–182, https://doi.org/10.1149/05049.0167ecst.
[43] S. Primdahl, M. Mogensen, Gas diffusion impedance in characterization of solid oxide fuel cell anodes, J. Electrochem. Soc. 146 (1999) 2827–2833, https://doi.org/10.1149/1.1392015.
[44] S. Primdahl, M. Mogensen, Gas conversion impedance: A test geometry effect in characterization of solid oxide fuel cell anode, J. Electrochem. Soc. 145 (1998) 2431–2438, https://doi.org/10.1149/1.1838654.